

Article

# A Multi-Input-Port Bidirectional DC/DC Converter for DC Microgrid Energy Storage System Applications

Binxin Zhu <sup>1,2,\*</sup> , Hui Hu <sup>1,2</sup>, Hui Wang <sup>1,2</sup> and Yang Li <sup>3</sup> 

<sup>1</sup> College of Electrical Engineering and New Energy, China Three Gorges University, Yichang 443000, China; huhuictgu@163.com (H.H.); wanghui@ctgu.edu.cn (H.W.)

<sup>2</sup> Hubei Provincial Key Laboratory for Operation and Control of Cascaded Hydropower Station, China Three Gorges University, Yichang 443000, China

<sup>3</sup> School of Automation, Wuhan University of Technology, Wuhan 430000, China; yang.li@whut.edu.cn

\* Correspondence: zhubinxin@ctgu.edu.cn; Tel.: +86-1719-765-0066

Received: 23 April 2020; Accepted: 26 May 2020; Published: 1 June 2020



**Abstract:** A multi-input-port bidirectional DC/DC converter is proposed in this paper for the energy storage systems in DC microgrid. The converter can connect various energy storage batteries to the DC bus at the same time. The proposed converter also has the advantages of low switch voltage stress and high voltage conversion gain. The working principle and performance characteristics of the converter were analyzed in detail, and a 200 W, two-input-port experimental prototype was built. The experimental results are consistent with the theoretical analysis.

**Keywords:** DC/DC converter; multi-input-port; bidirectional; energy storage

## 1. Introduction

Due to global issues like the greenhouse effect and energy shortage, renewable energy generation has developed rapidly in recent years [1–3]. Renewable energy generation is greatly affected by natural environmental factors, output power of which exhibits intermittence and randomness [4,5]. DC microgrid and energy storage systems, like batteries and supercapacitors, are usually used to smooth the fluctuating and stochastic output power of the renewable energy generation system [6,7]. A DC/DC converter with the capability of bidirectional energy conversion is the key device to connect batteries and the DC bus of the DC microgrid.

In recent years, many studies have been conducted on bidirectional DC/DC converters [8,9]. Many battery cells were connected in series to achieve high voltage [10]; however, a charge equalization circuit needs to be introduced to solve the problem of unbalanced battery charging [11]. On the contrary, many batteries can also be connected in parallel to achieve high reliability [12], but the output voltage of these batteries is low, and a high voltage gain converter is required in such an application [13,14]. Coupled inductors, switch capacitors, or voltage multiple cells can be used to improve the voltage conversion ratio [15–19]; however, most of the above converters are single input and single output, which means a large number of converters have to be used to connect each battery energy storage unit to the DC bus respectively [20,21], as Figure 1a shows.

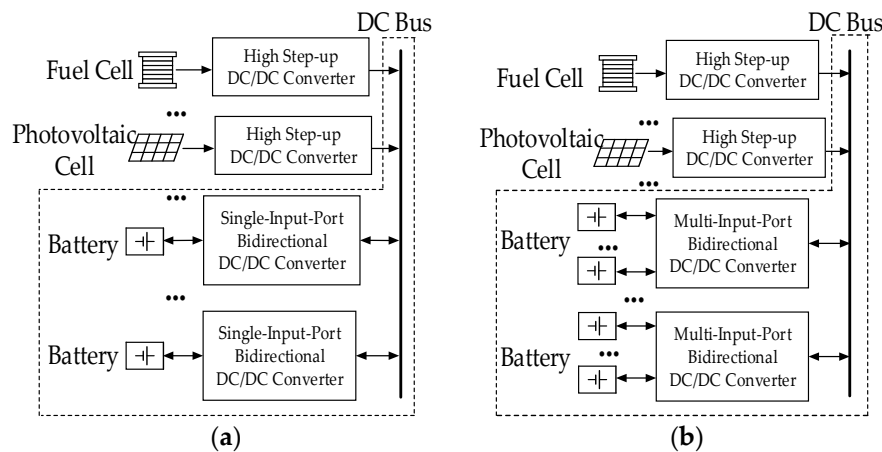


**Figure 1.** A DC microgrid with various battery energy storage systems. (a) traditional converters; (b) proposed converter.

In [22–24], some multi-input-port bidirectional converters have been presented; however, these converters have some common disadvantages, such as a large number of devices, large size, and high cost. A multi-input-port bidirectional DC/DC converter is proposed in this paper, many battery energy storage units can be connected to the DC bus by this converter together, as Figure 1b shows. Both in charging and discharging mode, the power flow to every battery can be controlled easily. Apparently, the cost of the whole system can be reduced.

The paper is organized as follows. The working principle, performance analysis, and extension of the proposed converter are described in Sections 2–4, respectively. In Section 5, the efficacy of the proposed converter is verified experimentally using a 200 W prototype.

## 2. Operation Principle of the Proposed Multi-Input-Port Bidirectional DC/DC Converter

The operation principle of the proposed converter will be presented in this section based on a topology with two input ports shown in Figure 2. To simplify the analysis, the following assumptions are made:

1. The currents  $i_{L1}$  and  $i_{L2}$  of the inductors  $L_1$  and  $L_2$  are both continuous.
2. All devices are ideal, regardless of the influence of parasitic parameters.
3. The switches  $S_1$  and  $S_2$  are regulated by an interleaved control strategy with the duty cycle greater than 0.5. While the switches  $Q_1$  and  $Q_2$  are controlled by an interleaved control strategy with the duty cycle less than 0.5. The operation principle of the converter can be analyzed based on the discharging or charging modes.

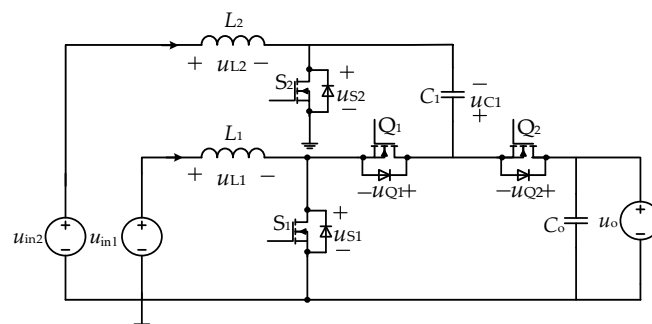


**Figure 2.** A multi-input-port bidirectional DC/DC converter for energy storage systems in a DC microgrid.

### 2.1. Discharging Mode (Boost)

In this mode,  $S_1$  and  $S_2$  are interleaved with  $180^\circ$  phase shift to turn on, and  $Q_1, Q_2$  are turned off. During a switching period  $T_s$ , there are three Sub-modes. The main waveforms of the converter working in steady state are shown in Figure 3, and the equivalent circuit of each Sub-mode is shown in Figure 4. The control signals of  $S_1$  and  $S_2$  are denoted by  $u_{gs1}$  and  $u_{gs2}$ , respectively.

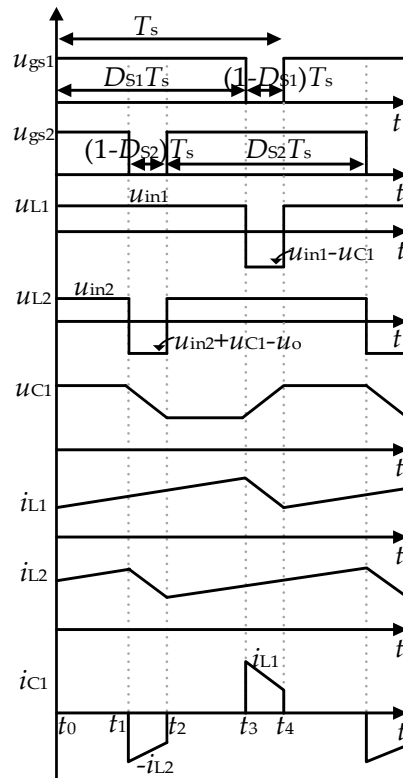


**Figure 3.** The main waveforms in one switching period  $T_s$ .

Sub-mode 1 [ $t_0-t_1, t_2-t_3$ ]: as Figure 4a shows,  $S_1$  and  $S_2$  are on. The voltages of the inductors  $L_1$  and  $L_2$  are equal to  $u_{in1}$  and  $u_{in2}$ , respectively. The inductor currents increase linearly at the rates of  $u_{in1}/L_1$  and  $u_{in2}/L_2$ , respectively. The current through the capacitor  $C_1$  is zero, while the capacitor voltage is unchanged.

Sub-mode 2 [ $t_1-t_2$ ]: as Figure 4b shows,  $S_1$  is on, and  $S_2$  is off. Same as Sub-mode 1, the voltage of the inductor  $L_1$  is still  $u_{in1}$ , and the current through it increases linearly at the rate of  $u_{in1}/L_1$ . However, the current through the inductor  $L_2$  decreases at the rate of  $(u_{in2} + u_{C1} - u_o)/L_2$ . The capacitor  $C_1$  is being discharged. The voltage of  $C_1$  decreases linearly, and the current of  $C_1$  is equal to  $i_{L2}$ .

Sub-mode 3 [ $t_3-t_4$ ]: as Figure 4c shows,  $S_1$  is off, and  $S_2$  is on. The current through the inductor  $L_1$  decreases at the rate of  $(u_{in1} - u_{C1})/L_1$ . The voltage of the inductor  $L_2$  is  $u_{in2}$ , and the current of  $L_2$  increases at the rate of  $u_{in2}/L_2$ . The capacitor  $C_1$  is being charged. The current of the capacitor  $C_1$  is equal to  $i_{L1}$ , and the voltage of  $C_1$  increases linearly.

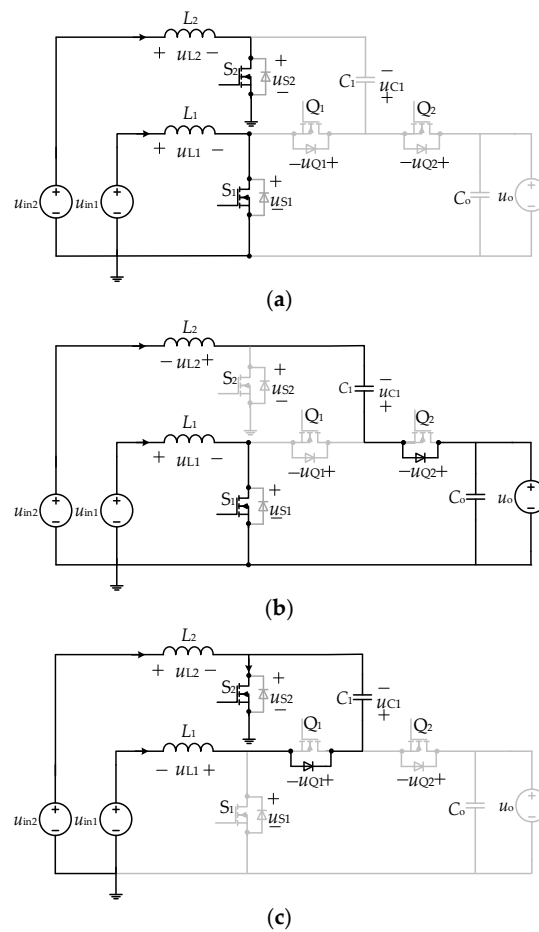


**Figure 4.** The equivalent circuits in the discharging mode for (a) Sub-mode 1; (b) Sub-mode 2; (c) Sub-mode 3.

## 2.2. Charging Mode (Buck)

In this mode,  $Q_1$  and  $Q_2$  are interleaved with  $180^\circ$  phase shift to turn on, and  $S_1, S_2$  are off. During a switching period  $T_s$ , there are three Sub-modes. The main waveforms of the converter working in steady state are shown in Figure 5, and the equivalent circuit of each Sub-mode is shown in Figure 6. The control signals of  $Q_1$  and  $Q_2$  are denoted by  $u_{gQ1}$  and  $u_{gQ2}$ , respectively.

Sub-mode 1 [ $t_0-t_1$ ]: as Figure 6a shows,  $Q_1$  is on, and  $Q_2$  is off. The current through the inductor  $L_1$  increases at the rate of  $(u_{C1} - u_{in1})/L_1$ . The voltage of the inductor  $L_2$  is  $u_{in2}$ , and the current of  $L_2$  decreases at the rate of  $u_{in2}/L_2$ . The capacitor  $C_1$  is being discharged. The voltage of  $C_1$  decreases linearly and the current of  $C_1$  is equal to  $i_{L1}$ .

Sub-mode 2 [ $t_1-t_2, t_3-t_4$ ]: as Figure 6b shows,  $Q_1$  and  $Q_2$  are off. The voltages of the inductors  $L_1$  and  $L_2$  are  $u_{in1}$  and  $u_{in2}$ , respectively. The inductor currents decrease linearly at the rates of  $u_{in1}/L_1$  and  $u_{in2}/L_2$ , respectively. The current through the capacitor  $C_1$  is zero, while the capacitor voltage is unchanged.

Sub-mode 3 [ $t_2-t_3$ ]: as Figure 6c shows,  $Q_1$  is off, and  $Q_2$  is on. The current of the inductor  $L_1$  decreases at the rate of  $u_{in1}/L_1$ . However, the current through the inductor  $L_2$  increases at the rate of  $(u_o - u_{in2} - u_{C1})/L_2$ . The capacitor  $C_1$  is being charged. The current of the capacitor  $C_1$  is equal to  $i_{L2}$ , and the voltage of  $C_1$  increases linearly.

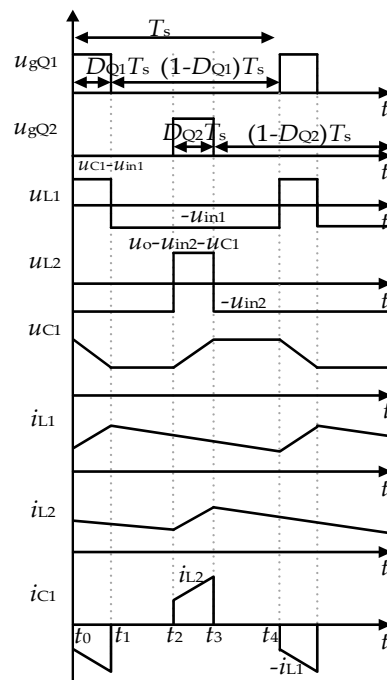


Figure 5. The main waveforms in one switching period  $T_s$ .

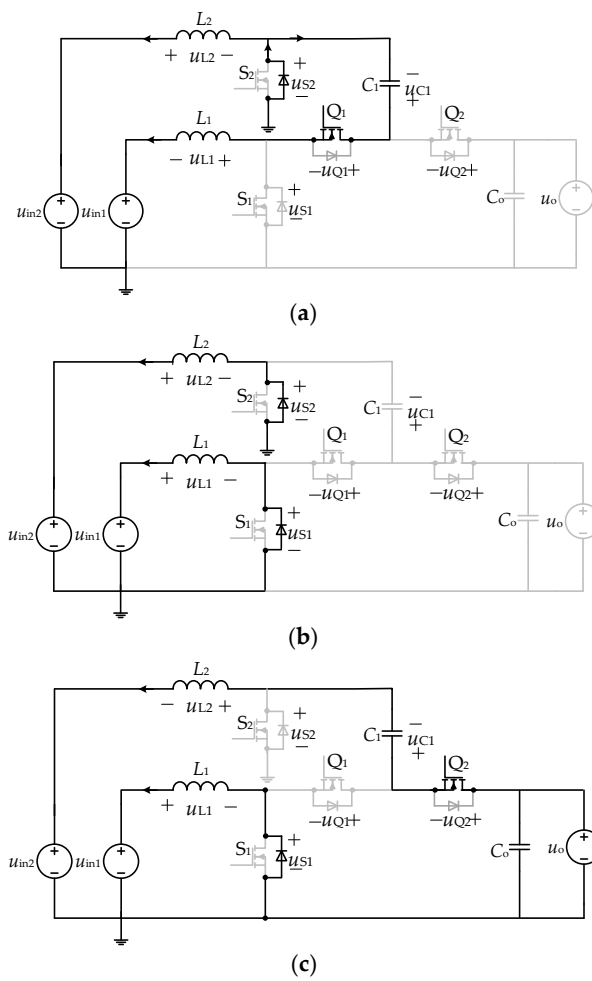


Figure 6. The equivalent circuits in the charging mode for (a) Sub-mode 1; (b) Sub-mode 2; (c) Sub-mode 3.

### 3. Performance Analysis

#### 3.1. Voltage Conversion Ratio

Discharging Mode (Boost): According to the analysis of the above working principle, the operating characteristics of the proposed converter can be derived from the three Sub-modes in one switching cycle  $T_s$ , based on the voltage-second balance of the inductors  $L_1$  and  $L_2$ .

$$D_{S1}u_{in1} + (1 - D_{S1})(u_{in1} - u_{C1}) = 0 \quad (1)$$

$$D_{S2}u_{in2} + (1 - D_{S2})(u_{in2} + u_{C1} - u_o) = 0 \quad (2)$$

From Equations (1) and (2), Equations (3) and (4) can be derived:

$$u_{C1} = \frac{u_{in1}}{1 - D_{S1}} \quad (3)$$

$$u_o = \frac{u_{in1}}{1 - D_{S1}} + \frac{u_{in2}}{1 - D_{S2}} \quad (4)$$

According to Equation (4), it can be clearly seen that the voltage conversion ratio of the proposed converter is twice that of the traditional boost converter.

When the input voltages  $u_{in1}$ ,  $u_{in2}$ , and the duty cycle  $D_{S1}$ ,  $D_{S2}$  are the same, respectively, the voltage conversion ratio of the proposed converter can be derived:

$$M_{\text{Boost}} = \frac{u_o}{u_{in}} = \frac{2}{1 - D_{\text{Boost}}} \quad (5)$$

Charging Mode (Buck): According to the analysis of the above working principle, the operating characteristics of the proposed converter can be derived from the Sub-three modes in one switching cycle  $T_s$ , based on the voltage-second balance of the inductors  $L_1$  and  $L_2$ .

$$D_{Q1}(u_{C1} - u_{in1}) + (1 - D_{Q1})(-u_{in1}) = 0 \quad (6)$$

$$D_{Q2}(u_o - u_{in2} - u_{C1}) + (1 - D_{Q2})(-u_{in2}) = 0 \quad (7)$$

From Equations (6) and (7), Equations (8) and (9) can be derived:

$$u_{C1} = \frac{u_{in1}}{D_{Q1}} \quad (8)$$

$$u_o = \frac{u_{in1}}{D_{Q1}} + \frac{u_{in2}}{D_{Q2}} \quad (9)$$

When the output voltages  $u_{in1}$ ,  $u_{in2}$ , and the duty cycle  $D_{Q1}$ ,  $D_{Q2}$  are the same, respectively, the voltage conversion ratio of the proposed converter can be derived:

$$M_{\text{Buck}} = \frac{u_{in}}{u_o} = \frac{D_{\text{Buck}}}{2} \quad (10)$$

According to Equation (10), it can be seen that the voltage conversion ratio of the proposed converter is half of that of the traditional buck converter.

#### 3.2. Relationship between the Currents of the Two Inductors

Discharging Mode (Boost): During a switching cycle  $T_s$ , in Sub-mode 3, the capacitor  $C_1$  is charged for  $(1 - D_{S1})T_s$  and the current of  $C_1$  is equal to  $i_{L1}$ . In Sub-mode 2, the capacitor  $C_1$  is discharged for

$(1 - D_{S2})T_s$ , and the current of  $C_1$  is equal to  $i_{L2}$ . In Sub-mode 1, the current of the capacitor  $C_1$  is zero. Due to the ampere-second balance of the capacitor  $C_1$ , the following can be derived:

$$I_{L1}(1 - D_{S1})T_s = I_{L2}(1 - D_{S2})T_s \quad (11)$$

$$I_{L1}(1 - D_{S1}) = I_{L2}(1 - D_{S2}) \quad (12)$$

When the duty cycles  $D_{S1}$  and  $D_{S2}$  are equal, the two input currents are also equal. Thus, automatic current sharing is realized. The power of the two ports can be adjusted through controlling  $D_{S1}$  and  $D_{S2}$ , respectively.

Charging Mode (Buck): During a switching cycle  $T_s$ , in Sub-mode 1, the capacitor  $C_1$  is discharged for  $D_{Q1}T_s$ , and the current of  $C_1$  is equal to  $i_{L1}$ . In Sub-mode 3, the capacitor  $C_1$  is charged for  $D_{Q2}T_s$ , and the current of  $C_1$  is equal to  $i_{L2}$ . In Sub-mode 2, the current of the capacitor  $C_1$  is zero. Due to the ampere-second balance of the capacitor  $C_1$ , the following can be derived:

$$I_{L1}D_{Q1}T_s = I_{L2}D_{Q2}T_s \quad (13)$$

$$I_{L1}D_{Q1} = I_{L2}D_{Q2} \quad (14)$$

When the duty cycle  $D_{Q1}$  and  $D_{Q2}$  are equal, the two input currents are also equal. Thus, automatic current sharing is realized. The power of the two ports can be adjusted through controlling  $D_{Q1}$  and  $D_{Q2}$ , respectively.

### 3.3. Voltage Stress of Switch

The voltage stresses of  $S_1$ ,  $S_2$ ,  $Q_1$ , and  $Q_2$  can be derived as follows:

#### 1. Discharging Mode (Boost):

$$u_{S1} = u_{C1} \quad (15)$$

$$u_{S2} = u_{Q2} = u_o - u_{C1} \quad (16)$$

$$u_{Q1} = u_o \quad (17)$$

#### 2. Charging Mode (Buck):

$$u_{S1} = u_{C1} \quad (18)$$

$$u_{S2} = u_{Q2} = u_o - u_{C1} \quad (19)$$

$$u_{Q1} = u_o \quad (20)$$

### 3.4. Current Stress of Switch

Discharging Mode (Boost): To begin with the time of  $S_1$  turning on, in the following cycle  $T_s$ , the inductor currents  $i_{L1}$ ,  $i_{L2}$  can be represented as

$$i_{L1} = \begin{cases} I_{L1} - \frac{u_{in1}D_{S1}T_s}{2L_1} + \frac{u_{in1}}{L_1}t, & 0 < t \leq D_{S1}T_s \\ I_{L1} + \frac{u_{in1}D_{S1}T_s}{2L_1} - \frac{u_{C1} - u_{in1}}{L_1}t, & D_{S1}T_s < t \leq T_s \end{cases} \quad (21)$$

$$i_{L2} = \begin{cases} I_{L2} + \frac{1-D_{S2}}{2L_2}u_{in2}T_s + \frac{u_{in2}}{L_2}t, & 0 < t \leq (D_{S2} - \frac{1}{2})T_s \\ I_{L2} + \frac{u_{in2}D_{S2}T_s}{2L_2} - \frac{u_o - u_{C1} - u_{in2}}{L_2}[t - (D_{S2} - \frac{1}{2})T_s], & (D_{S2} - \frac{1}{2})T_s < t \leq \frac{T_s}{2} \\ I_{L2} - \frac{u_{in2}D_{S2}T_s}{2L_2} + \frac{u_{in2}}{L_2}(t - \frac{T_s}{2}), & \frac{T_s}{2} < t \leq T_s \end{cases} \quad (22)$$

According to the three Sub-modes of the circuit, in a switching cycle, the currents through  $S_1$  and  $S_2$  at every stage can be derived as follows:

$$i_{S1} = \begin{cases} i_{L1}, & 0 < t \leq D_{S1}T_s \\ 0, & D_{S1}T_s < t \leq T_s \end{cases} \quad (23)$$

$$i_{S2} = \begin{cases} i_{L2}, & 0 < t \leq (D_{S2} - \frac{1}{2})T_s \\ 0, & (D_{S2} - \frac{1}{2})T_s < t \leq \frac{T_s}{2} \\ i_{L2}, & \frac{T_s}{2} < t \leq D_{S2}T_s \\ i_{L1} + i_{L2}, & D_{S2}T_s < t \leq T_s \end{cases} \quad (24)$$

From Equations (21)–(24), the currents through  $S_1$ ,  $S_2$ ,  $Q_1$ , and  $Q_2$  can be derived as follows:

$$i_{S1} = i_{Q1} = I_{L1} + \frac{u_{in1}D_{S1}T_s}{2L_1} \quad (25)$$

$$i_{S2} = I_{L1} + \frac{u_{in1}D_{S1}T_s}{2L_1} + I_{L2} + \frac{D_{S2} - 1}{2L_2}u_{in2}T_s \quad (26)$$

$$i_{Q2} = I_{L2} + \frac{u_{in2}D_{S2}T_s}{2L_2} \quad (27)$$

Charging Mode (Buck): To begin with the time of  $Q_1$  turning on, in the following cycle  $T_s$ , the inductor currents  $i_{L1}$  and  $i_{L2}$  can be denoted by

$$i_{L1} = \begin{cases} \frac{u_{C1} - u_{in1}}{L_1}t, & 0 < t \leq D_{Q1}T_s \\ I_{L1} + \frac{(u_{C1} - u_{in1})D_{Q1}T_s}{2L_1} - \frac{u_{in1}}{L_1}(t - D_{Q1}T_s), & D_{Q1}T_s < t \leq T_s \end{cases} \quad (28)$$

$$i_{L2} = \begin{cases} I_{L2} + \frac{(u_o - u_{C1} - u_{in2})D_{Q2}T_s}{2L_2} - \frac{u_{in2}}{L_2}(\frac{1}{2} - D_{Q2})T_s - \frac{u_{in2}}{L_2}t, & 0 < t \leq \frac{1}{2}T_s \\ I_{L2} - \frac{(u_o - u_{C1} - u_{in2})D_{Q2}T_s}{2L_2} + \frac{(u_o - u_{C1} - u_{in2})}{L_2}(t - \frac{1}{2}T_s), & \frac{1}{2}T_s < t \leq (\frac{1}{2} + D_{Q2})T_s \\ I_{L2} + \frac{(u_o - u_{C1} - u_{in2})D_{Q2}T_s}{2L_2} - \frac{u_{in2}}{L_2}[t - (\frac{1}{2} + D_{Q2})T_s], & (\frac{1}{2} + D_{Q2})T_s < t \leq T_s \end{cases} \quad (29)$$

According to the three Sub-modes of the circuit, in a switching cycle, the currents through  $Q_1$  and  $Q_2$  at each stage can be derived as follows:

$$i_{Q1} = \begin{cases} i_{L1}, & 0 < t \leq D_{Q1}T_s \\ 0, & D_{Q1}T_s < t \leq T_s \end{cases} \quad (30)$$

$$i_{Q2} = \begin{cases} 0, & 0 < t \leq \frac{1}{2}T_s \\ i_{L2}, & \frac{1}{2}T_s < t \leq (\frac{1}{2} + D_{Q2})T_s \\ 0, & (\frac{1}{2} + D_{Q2})T_s < t \leq T_s \end{cases} \quad (31)$$

From Equations (28)–(31), the currents through  $S_1$ ,  $S_2$ ,  $Q_1$ , and  $Q_2$  can be derived as follows:

$$i_{S1} = i_{Q1} = I_{L1} + \frac{u_{in1}(1 - D_{Q1})T_s}{2L_1} \quad (32)$$

$$i_{Q2} = I_{L2} + \frac{u_{in2}(1 - D_{Q2})T_s}{2L_2} \quad (33)$$

$$i_{S2} = I_{L1} + \frac{u_{in1}(1 - D_{Q1})T_s}{2L_1} + I_{L2} - \frac{u_{in2}(1 - D_{Q2})T_s}{2L_2} + \frac{u_{in2}}{L_2}(\frac{1}{2} - D_{Q1})T_s \quad (34)$$

### 3.5. Power Flow

Discharging Mode (Boost): The inductor current  $i_{L1}$  increases as the duty cycle  $D_{S1}$  increases, and the inductor current  $i_{L2}$  decreases as the duty cycle  $D_{S2}$  decreases. Since the two input voltages  $u_{in1}$ ,  $u_{in2}$  are equal, the ratio of the power of the two ports is equal to the ratio of the two inductor currents. Therefore, when  $D_{S1} < D_{S2}$ ,  $i_{L1} < i_{L2}$ ,  $i_{L1}/i_{L2} < 1$ ; when  $D_{S1} = D_{S2}$ ,  $i_{L1} = i_{L2}$ ,  $i_{L1}/i_{L2} = 1$ ; when  $D_{S1} > D_{S2}$ ,  $i_{L1} > i_{L2}$ ,  $i_{L1}/i_{L2} > 1$ . Making  $D_{S1}$ : 0.5–0.8 as the  $x$ -axis,  $D_{S2}$ : 0.8–0.5 as the  $y$ -axis, and  $i_{L1}/i_{L2}$  as the  $z$ -axis, the following three-dimensional figure can be obtained as Figure 7 shows.

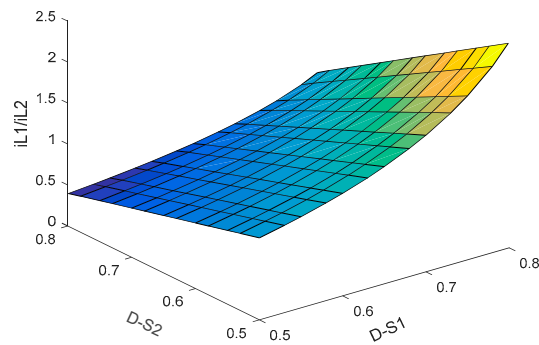


Figure 7.  $i_{L1}/i_{L2}$  3D graph (Discharging Mode (Boost)).

Charging Mode (Buck): The inductor current  $i_{L1}$  increases as the duty cycle  $D_{Q1}$  decreases, and the inductor current  $i_{L2}$  decreases as the duty cycle  $D_{Q2}$  increases. Since the two output voltages  $u_{in1}$ ,  $u_{in2}$  are equal, the ratio of the power of the two ports is equal to the ratio of the two inductor currents. Therefore, when  $D_{Q1} < D_{Q2}$ ,  $i_{L1} > i_{L2}$ ,  $i_{L1}/i_{L2} > 1$ ; when  $D_{Q1} = D_{Q2}$ ,  $i_{L1} = i_{L2}$ ,  $i_{L1}/i_{L2} = 1$ ; when  $D_{Q1} > D_{Q2}$ ,  $i_{L1} < i_{L2}$ ,  $i_{L1}/i_{L2} < 1$ . Making  $D_{Q1}$ : 0.5–0.2 as the  $x$ -axis,  $D_{Q2}$ : 0.2–0.5 as the  $y$ -axis, and  $i_{L1}/i_{L2}$  as the  $z$ -axis, the following three-dimensional figure can be obtained as Figure 8 shows.

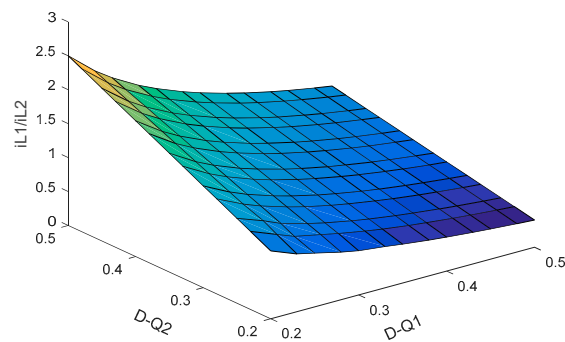


Figure 8.  $i_{L1}/i_{L2}$  3D graph (Charging Mode (Buck)).

### 3.6. Comparison of the Proposed Converter with Other Converters

Some quantitative comparisons between some existing multi-input-port topologies, and the proposed converter are given in Table 1. As can be seen, compared to [22–24], the number of devices of the proposed converter is less, which means fewer losses and a lower cost.

Table 1. Comparison of the converters.

	[22]	[23]	[24]	Proposed
No. of ports	3	4	3	3
No. of switches	12	4	6	4
No. of diodes	0	4	0	0
No. of inductors	6	4	2	2
No. of capacitors	3	5	2	2

### 4. Extension of the Topology

#### 4.1. Topology of the N-Input-Port Bidirectional DC/DC Converter

Based on the topology of the two-input-port bidirectional DC/DC converter shown in Figure 2, the n-input-port bidirectional DC/DC converter topology can be derived as Figure 9 shows. To simplify, assumptions are made as follows:

1. Currents of the inductors  $i_{L1}$ ,  $i_{L2}$ , ..., and  $i_{Ln}$  are all continuous.
2. All devices are ideal, regardless of the influence of parasitic parameters.
3. Discharging Mode (Boost): during a switching period  $T_s$ ,  $S_1, S_2, \dots$ , and  $S_n$  interleaved with  $360^\circ/n$  phase shift are turned on with the duty cycle greater than  $(1 - 1/n)$ , and  $Q_1, Q_2, \dots$ , and  $Q_n$  are turned off. Charging Mode (Buck): during a switching period  $T_s$ ,  $Q_1, Q_2, \dots$ , and  $Q_n$  interleaved with  $360^\circ/n$  phase shift are turned on with the duty cycle less than  $1/n$ , and  $S_1, S_2, \dots$ , and  $S_n$  are turned off.

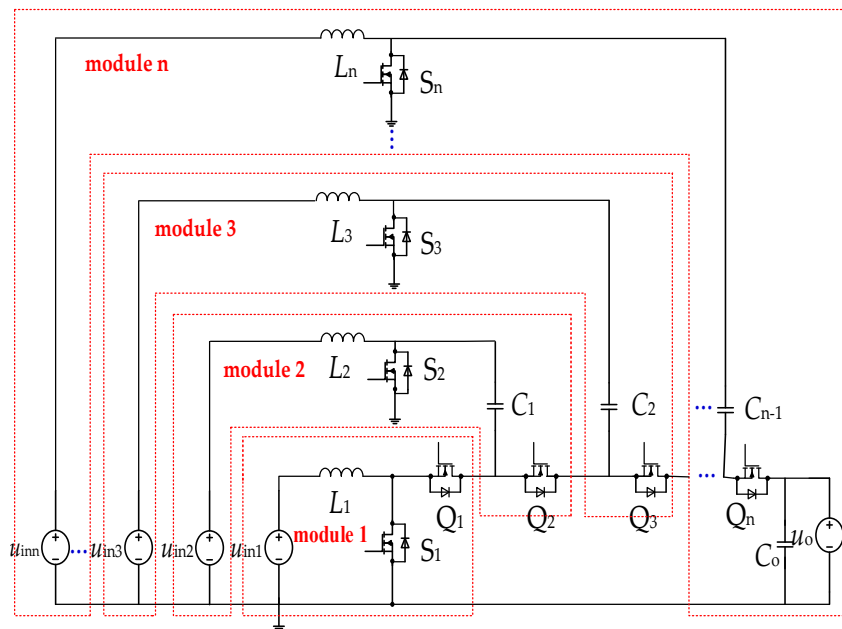


Figure 9. An n-input-port bidirectional DC/DC converter for DC microgrid energy storage system.

#### 4.2. Voltage Conversion Ratio

Discharging Mode (Boost): Due to the voltage-second balance of the inductors  $L_1, L_2, \dots$ , and  $L_n$ , it can be derived:

$$D_{S(i-1)}u_{in(i-1)} = (1 - D_{S(i-1)})(u_{C(i-1)} - u_{C(i-2)} - u_{in(i-1)}) \tag{35}$$

$$D_{S_i}u_{ini} = (1 - D_{S_i})(u_o - u_{C(i-1)} - u_{ini}) \tag{36}$$

$$u_{C_i} = \sum_{p=1}^i \frac{u_{inp}}{1 - D_{S_p}} \quad (1 \leq i \leq n - 1) \tag{37}$$

$$u_o = \sum_{i=1}^n \frac{u_{ini}}{1 - D_{S_i}} \tag{38}$$

When  $D_{S_1} = D_{S_2} = \dots = D_{S_n} = D_{Boost}$ , the ratio of the output voltage  $u_o$ , and each input voltage  $u_{ini}$  is the voltage gain  $M_i$  of each input port.

$$M_i = \frac{u_o}{u_{ini}} \tag{39}$$

$$\sum_{i=1}^n \frac{u_{ini}}{u_o} = 1 - D_{\text{Boost}} \quad (40)$$

$$\frac{1}{M_1} + \frac{1}{M_2} + \dots + \frac{1}{M_n} = 1 - D_{\text{Boost}} \quad (41)$$

When  $u_{in1} = u_{in2} = \dots = u_{inn}$ ,

$$M_1 = M_2 = \dots = M_n = \frac{n}{1 - D_{\text{Boost}}} \quad (42)$$

Charging Mode (Buck): Due to the voltage-second balance of the inductors  $L_1, L_2, \dots$ , and  $L_n$ , it can be derived:

$$(1 - D_{Q(i-1)})u_{in(i-1)} = D_{Q(i-1)}(u_{C(i-1)} - u_{C(i-2)} - u_{in(i-1)}) \quad (43)$$

$$(1 - D_{Qi})u_{ini} = D_{Qi}(u_o - u_{C(i-1)} - u_{ini}) \quad (44)$$

$$u_{Ci} = \sum_{p=1}^i \frac{u_{inp}}{D_{Qp}} \quad (1 \leq i \leq n - 1) \quad (45)$$

$$u_o = \sum_{i=1}^n \frac{u_{ini}}{D_{Qi}} \quad (46)$$

When  $D_{Q1} = D_{Q2} = \dots = D_{Qn} = D_{\text{Buck}}$ , the ratio of each output voltage  $u_{ini}$  and the input voltage  $u_o$  is the voltage gain  $M_i$  of each output port.

$$M_i = \frac{u_{ini}}{u_o} \quad (47)$$

$$\sum_{i=1}^n \frac{u_{ini}}{u_o} = D_{\text{Buck}} \quad (48)$$

$$M_1 + M_2 + \dots + M_n = D_{\text{Buck}} \quad (49)$$

When  $u_{in1} = u_{in2} = \dots = u_{inn}$ ,

$$M_1 = M_2 = \dots = M_n = \frac{D_{\text{Buck}}}{n} \quad (50)$$

#### 4.3. Relationship between the Currents of the Inductors

It is assumed that the average values of the inductor currents  $i_{L1}, i_{L2}, \dots$ , and  $i_{Ln}$  are  $I_{L1}, I_{L2}, \dots$ , and  $I_{Ln}$ , respectively.

Discharging Mode (Boost): Due to the ampere-second balance of the capacitors  $C_1, C_2, \dots$ , and  $C_n$ , it can be derived as follows:

$$I_{L1}(1 - D_{S1}) = I_{L2}(1 - D_{S2}) = \dots = I_{Ln}(1 - D_{Sn}) \quad (51)$$

When  $D_{S1} = D_{S2} = \dots = D_{Sn}$ ,  $I_{L1} = I_{L2} = \dots = I_{Ln}$ . Thus, automatic current sharing is realized. The power of all the ports can be adjusted through controlling  $D_{S1}, D_{S2}, \dots$ , and  $D_{Sn}$ , respectively.

Charging Mode (Buck): Due to the ampere-second balance of the capacitors  $C_1, C_2, \dots$ , and  $C_n$ , it can be derived:

$$I_{L1}D_{Q1} = I_{L2}D_{Q2} = \dots = I_{Ln}D_{Qn} \quad (52)$$

When  $D_{Q1} = D_{Q2} = \dots = D_{Qn}$ ,  $I_{L1} = I_{L2} = \dots = I_{Ln}$ . Thus, automatic current sharing is realized. The power of all the ports can be adjusted through controlling  $D_{Q1}, D_{Q2}, \dots$ , and  $D_{Qn}$ , respectively.

In practical applications, the efficiency of the converter will drop along with the increase in the number of input ports.

## 5. Experimental Results

To verify the analysis presented in the previous sections, experiments were conducted based on a 200 W two-input-port prototype developed from the proposed converter. The specification of the prototype is given in Table 2, and the experimental results are presented and discussed as follows.

**Table 2.** Specification of the prototype.

Parameters	Values
Voltage ( $u_{in1}$ , $u_{in2}$ )	24 V
Voltage ( $u_o$ )	200 V
Output power ( $P_o$ )	200 W
Switching frequency ( $f_s$ )	100 kHz
Switch ( $S_1$ , $S_2$ , $Q_1$ , $Q_2$ )	C3M0280090D
Capacitors	$C_o$ : 10 $\mu$ F, $C_1$ : 4 $\mu$ F
Inductors ( $L_1$ , $L_2$ )	400 $\mu$ H

### 5.1. Constant Duty Cycle

Discharging Mode (Boost): Figure 10a shows the waveforms of  $u_{gs1}$ ,  $u_{gs2}$ ,  $u_{in1}$ , and  $u_{in2}$ , where the duty cycles are around 0.76. Figure 10b shows the waveforms of  $u_o$ ,  $u_{C_o}$ , and  $u_{C_1}$ . It can be seen that the DC values of  $u_{C_1}$  and  $u_o$  are about 100 V and 200 V, respectively. The voltage conversion gain is around 8.3, which is consistent with that calculated by Equation (5). Figure 10c shows that the voltage stresses of  $S_1$ ,  $S_2$ , and  $Q_2$  are all about 100 V, while the voltage stress of  $Q_1$  is about 200 V. These are consistent with that obtained by Equations (15)–(17). Figure 10d shows that the currents of  $L_1$  and  $L_2$  are both about 4 A. Apparently, the measured results are all consistent with the previous analysis.

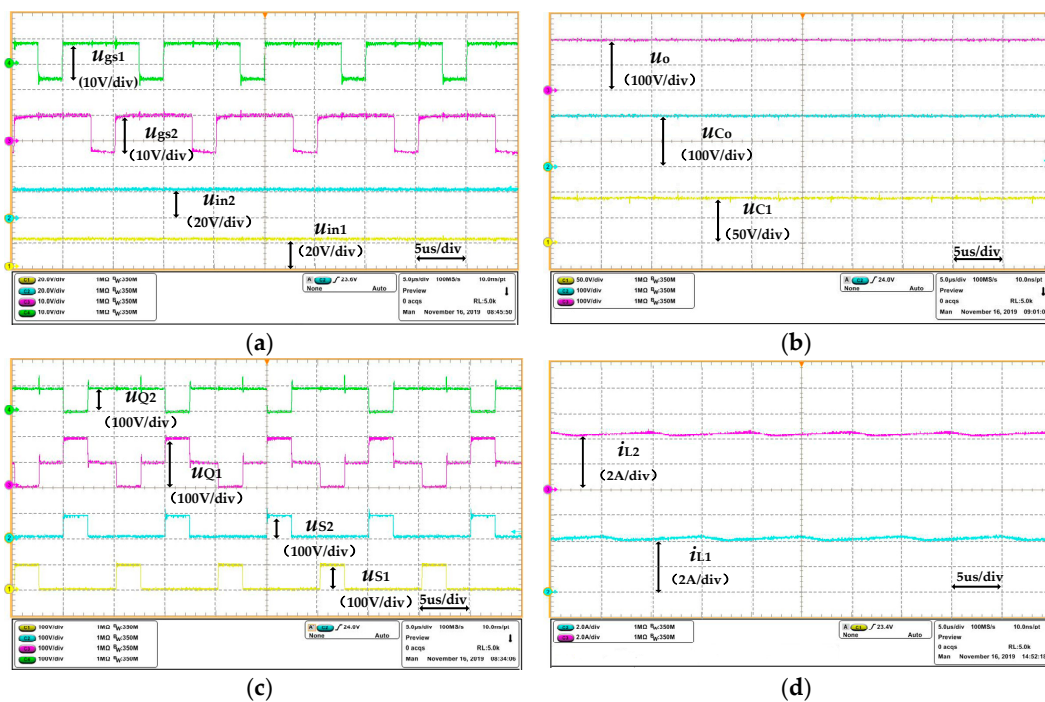


**Figure 10.** The waveforms of the experimental prototype. (a) driving waveforms of the switches and waveforms of the input voltage. (b) waveforms of voltages of  $C_o$ ,  $C_1$ , and the waveform of the output voltage. (c) waveforms of voltages of the switches. (d) waveforms of currents of the inductors.

Charging Mode (Buck): Figure 11a shows the waveforms of  $u_{gQ1}$ ,  $u_{gQ2}$ ,  $u_{in1}$ , and  $u_{in2}$ , the duty cycles are near 0.24. Figure 11b shows the waveforms of  $u_o$ ,  $u_{Co}$ , and  $u_{C1}$ ; it can be seen that the DC values of  $u_{C1}$ ,  $u_o$  are about 100 V, 200 V, and the conversion gain is approximately 0.12, which is consistent with Equation (10). Figure 11c shows voltage stresses of  $S_1$ ,  $S_2$ ,  $Q_2$  are nearly 100 V, and the voltage stress of  $Q_1$  is about 200 V, which are consistent with Equations (18)–(20). Figure 11d shows the waveforms of  $i_{L1}$ ,  $i_{L2}$ . The DC values of  $i_{L1}$ ,  $i_{L2}$  are both about 4 A; evidently, the measured results are all consistent with the theoretical analysis.

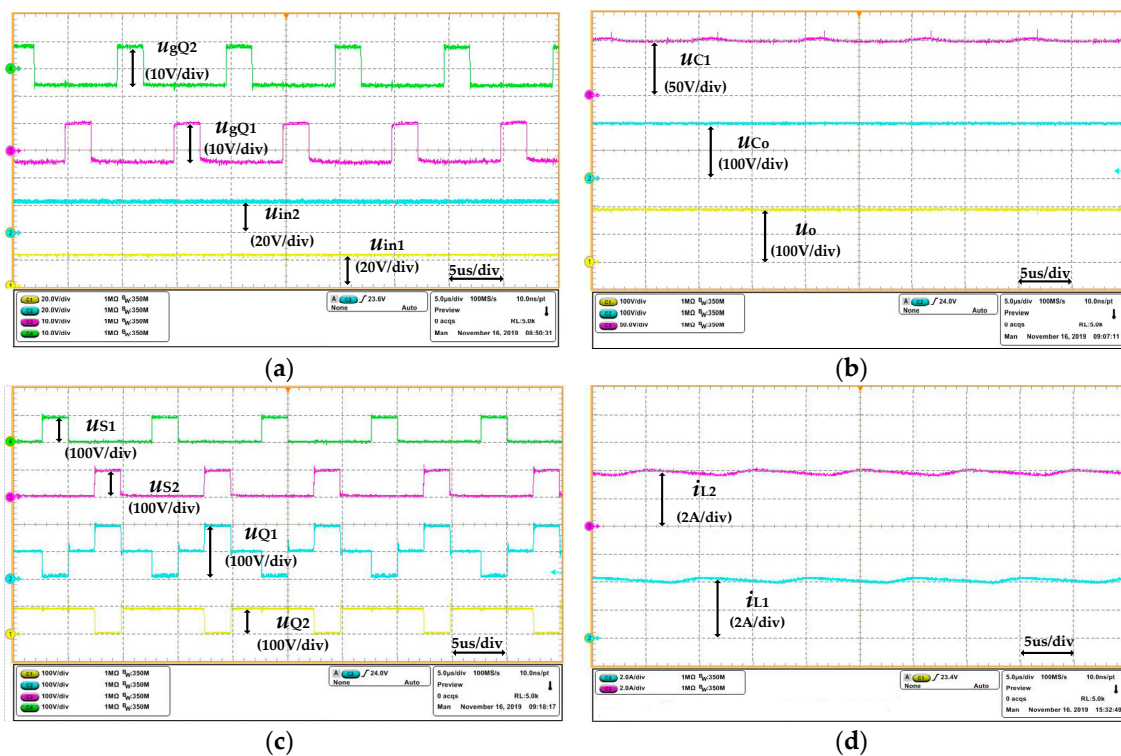


**Figure 11.** The waveforms of the experimental prototype. (a) driving waveforms of the switches and waveforms of the output voltage. (b) waveforms of voltages of  $C_o$ ,  $C_1$ , and the waveform of the input voltage. (c) waveforms of voltages of the switches. (d) waveforms of currents of the inductors.

### 5.2. Varying Duty Cycle

Discharging Mode (Boost): Figure 12a shows the changes of  $i_{L1}$  and  $i_{L2}$  when the duty cycle  $D_{S1}$  and  $D_{S2}$  are adjusted. With the increase of the duty cycle, the inductor current increases, and the power of the branch circuit increases.

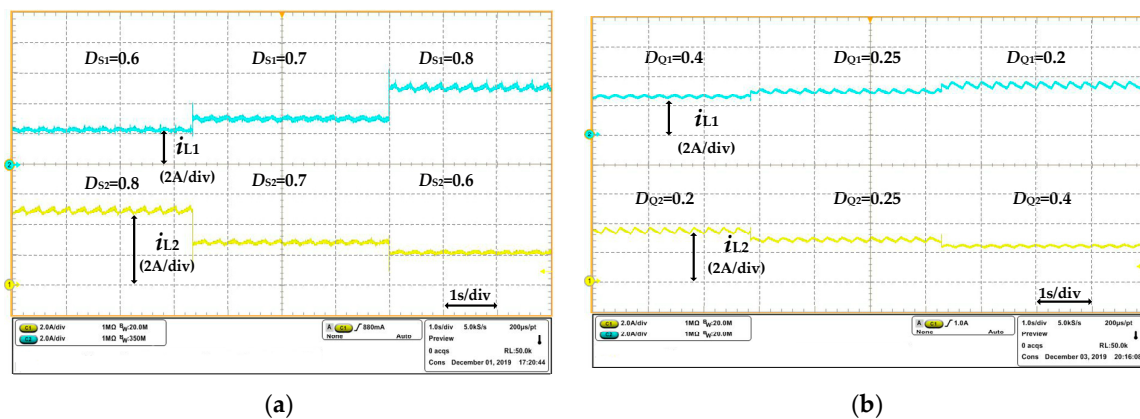


**Figure 12.** Power flow diagram for (a) discharging mode (Boost); (b) charging mode (Buck).

Charging Mode (Buck): Figure 12b shows the changes of  $i_{L1}$  and  $i_{L2}$  when the duty cycle  $D_{Q1}$  and  $D_{Q2}$  are adjusted. With the increase of the duty cycle, the inductor current decreases, and the power of the branch circuit decreases.

### 5.3. Converter Efficiency and Conversion Ratio

Based on the experimental results, the converter efficiency and the conversion ratio are analyzed and presented in this sub-section.

Discharging Mode (Boost): Figure 13a shows the curve of efficiency changing with output voltage after changing the duty cycle and the curve of efficiency changing with output power after changing the load. The calculated loss distribution of the experimental prototype is shown in Figure 13b. The main losses are switching losses 9.59 W, anti-parallel diode losses 3.6 W, and inductor losses 2.874 W. As is shown in Figure 13c, the voltage conversion ratio changes with the duty cycle. When the duty cycle is more than 0.7, the difference between the actual gain and the theoretical gain gradually increases as the duty cycle increases.

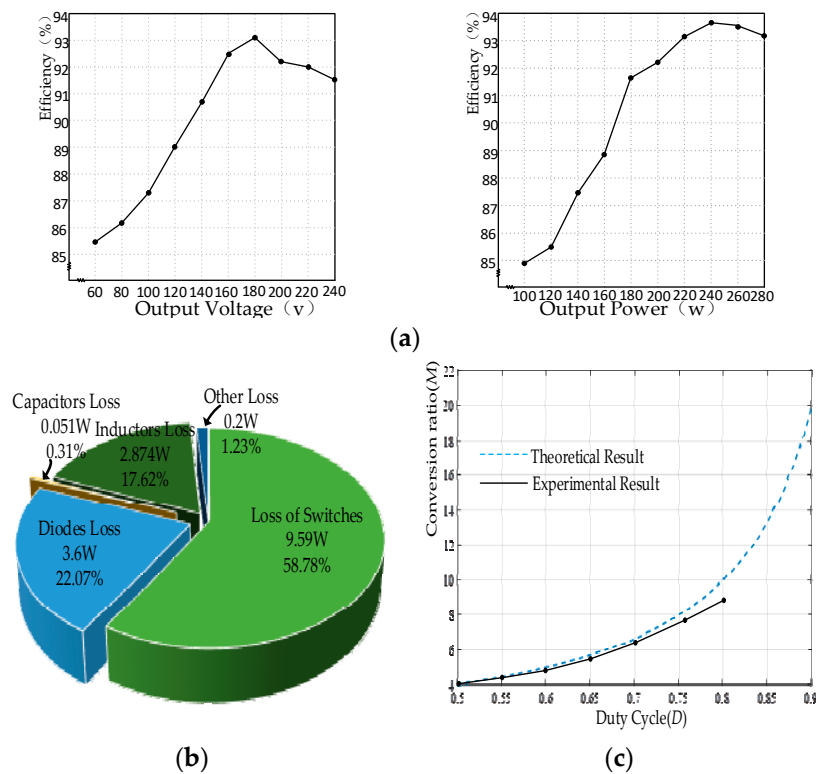


**Figure 13.** Discharging mode (Boost): (a) efficiency curves of the prototype; (b) loss distribution of the prototype; (c) conversion ratio ( $M$ ) vs. duty cycle ( $D$ ) graph.

Charging Mode (Buck): Figure 14a shows the curve of efficiency changing with output voltage after changing the duty cycle and the curve of efficiency changing with output power after changing the load. The calculated loss distribution of the experimental prototype is shown in Figure 14b. The main losses are anti-parallel diode losses 9 W, switching losses 4.38 W, and inductor losses 2.874 W. As is shown in Figure 14c, the voltage conversion ratio changes with the duty cycle. When the duty cycle is less than 0.3, the difference between the actual gain and the theoretical gain gradually increases as the duty cycle decreases.

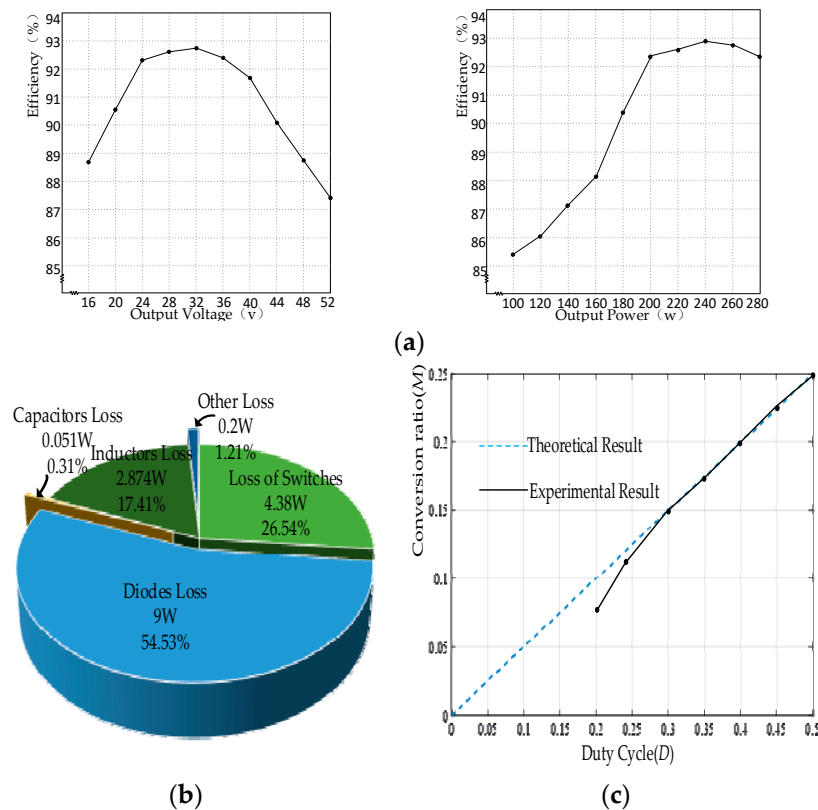


**Figure 14.** Charging mode (Buck): (a) efficiency curves of the prototype; (b) loss distribution of the prototype; (c) conversion ratio ( $M$ ) vs. duty cycle ( $D$ ) graph.

## 6. Conclusions

A multi-input-port bidirectional DC/DC converter for DC microgrid energy storage system applications is proposed in this paper. Comprehensive analyses on the working principle and performance of the proposed converter are given. Experimental results are presented, and it is verified that, compared to the traditional buck and boost converter, the proposed bidirectional converter has the following advantages: (1) a wider range of voltage conversion can be achieved and the voltage stresses of the switches are lower; (2) the power flow of each port can be adjusted easily through the controlling of duty cycles; (3) the number of input ports of the proposed converter can be expanded, which makes it more applicable.

**Author Contributions:** Conceptualization, B.Z.; methodology, B.Z. and H.H.; software, B.Z. and H.H.; writing—original draft preparation, H.H.; writing—review and editing, B.Z. and H.H.; supervision, H.W. and Y.L.; funding acquisition, B.Z. All authors have read and agreed to the published version of the manuscript.

**Funding:** This research was funded by the National Natural Science Foundation of China, grant number 51707103.

**Conflicts of Interest:** The authors declare no conflict of interest.

## References

1. Wu, Y.-E.; Hsu, K.-C. Novel Three-Port Bidirectional DC/DC Converter with Three-Winding Coupled Inductor for Photovoltaic System. *Energies* **2020**, *13*, 1132. [[CrossRef](#)]
2. Zhu, B.; Zeng, Q.; Chen, Y.; Zhao, Y.; Liu, S. A Dual-Input High Step-Up DC/DC Converter with ZVT Auxiliary Circuit. *IEEE Trans. Energy Convers.* **2018**, *34*, 161–169. [[CrossRef](#)]
3. Zhu, B.; Ding, F.; Vilathgamuwa, D.M. Coat Circuits for DC–DC Converters to Improve Voltage Conversion Ratio. *IEEE Trans. Power Electron.* **2020**, *35*, 3679–3687. [[CrossRef](#)]

4. Wang, C.; Li, X.; Tian, T.; Xu, Z.; Chen, R. Coordinated Control of Passive Transition from Grid-Connected to Islanded Operation for Three/Single-Phase Hybrid Multimicrogrids Considering Speed and Smoothness. *IEEE Trans. Ind. Electron.* **2020**, *67*, 1921–1931. [[CrossRef](#)]
5. Li, Y.; Vilathgamuwa, D.M.; Choi, S.S.; Xiong, B.; Tang, J.; Su, Y.; Wang, Y. Design of minimum cost degradation-conscious lithium-ion battery energy storage system to achieve renewable power dispatchability. *Appl. Energy* **2020**, *260*, 114282. [[CrossRef](#)]
6. Xu, G.; Xu, L.; Yao, L. Wind turbines output power smoothing using embedded energy storage systems. *J. Mod. Power Syst. Clean Energy* **2013**, *1*, 49–57. [[CrossRef](#)]
7. Li, Z.H.; Xiang, X.; Hu, T.H.; Abu-Siada, A.; Li, Z.X.; Xu, Y.C. An improved digital integral algorithm to enhance the measurement accuracy of Rogowski coil-based electronic transformers. *INT J. Elec. Power* **2020**, *118*, 105806. [[CrossRef](#)]
8. Lai, C.-M.; Cheng, Y.-H.; Hsieh, M.-H.; Lin, Y.-C. Development of a Bidirectional DC/DC Converter with Dual-Battery Energy Storage for Hybrid Electric Vehicle System. *IEEE Trans. Veh. Technol.* **2018**, *67*, 1036–1052. [[CrossRef](#)]
9. Wai, R.-J.; Zhang, Z.-F. Design of High-Efficiency Isolated Bidirectional DC/DC Converter with Single-Input Multiple-Outputs. *IEEE Access* **2019**, *7*, 87543–87560. [[CrossRef](#)]
10. Park, H.-S.; Kim, C.-E.; Kim, C.-H.; Moon, G.-W.; Lee, J.-H. A Modularized Charge Equalizer for an HEV Lithium-Ion Battery String. *IEEE Trans. Ind. Electron.* **2009**, *56*, 1464–1476. [[CrossRef](#)]
11. Anno, T.; Koizumi, H. Double-Input Bidirectional DC/DC Converter Using Cell-Voltage Equalizer with Flyback Transformer. *IEEE Trans. Power Electron.* **2014**, *30*, 2923–2934. [[CrossRef](#)]
12. Ibanez, F.; Echeverria, J.M.; Vadillo, J.; Fontan, L. High-Current Rectifier Topology Applied to a 4-kW Bidirectional DC–DC Converter. *IEEE Trans. Ind. Appl.* **2013**, *50*, 68–77. [[CrossRef](#)]
13. Duan, R.-Y.; Lee, J.-D. High-efficiency bidirectional DC-DC converter with coupled inductor. *IET Power Electron.* **2012**, *5*, 115–123. [[CrossRef](#)]
14. Zhou, L.-W.; Zhu, B.-X.; Luo, Q.-M. High step-up converter with capacity of multiple input. *IET Power Electron.* **2012**, *5*, 524–531. [[CrossRef](#)]
15. Saadat, P.; Abbaszadeh, K. A Single-Switch High Step-Up DC–DC Converter Based on Quadratic Boost. *IEEE Trans. Ind. Electron.* **2016**, *63*, 7733–7742. [[CrossRef](#)]
16. Hsieh, Y.-P.; Chen, J.-F.; Yang, L.-S.; Wu, C.-Y.; Liu, W.-S. High-Conversion-Ratio Bidirectional DC–DC Converter with Coupled Inductor. *IEEE Trans. Ind. Electron.* **2013**, *61*, 210–222. [[CrossRef](#)]
17. Zhang, Y.; Liu, H.; Li, J.; Sumner, M.; Xia, C. DC–DC Boost Converter with a Wide Input Range and High Voltage Gain for Fuel Cell Vehicles. *IEEE Trans. Power Electron.* **2019**, *34*, 4100–4111. [[CrossRef](#)]
18. Wu, G.; Ruan, X.; Ye, Z. Nonisolated High Step-Up DC–DC Converters Adopting Switched-Capacitor Cell. *IEEE Trans. Ind. Electron.* **2014**, *62*, 383–393. [[CrossRef](#)]
19. Zhu, B.; Wang, H.; Vilathgamuwa, D.M.; Vilathgamuwa, M. Single-switch high step-up boost converter based on a novel voltage multiplier. *IET Power Electron.* **2019**, *12*, 3732–3738. [[CrossRef](#)]
20. Varesi, K.; Hosseini, S.H.; Sabahi, M.; Babaei, E.; Vosoughi, N. Performance and design analysis of an improved non-isolated multiple input buck DC–DC converter. *IET Power Electron.* **2017**, *10*, 1034–1045. [[CrossRef](#)]
21. Mangu, B.; Akshatha, S.; Suryanarayana, D.; Fernandes, B.G.; Bhukya, M. Grid-Connected PV-Wind-Battery-Based Multi-Input Transformer-Coupled Bidirectional DC-DC Converter for Household Applications. *IEEE J. Emerg. Sel. Top. Power Electron.* **2016**, *4*, 1086–1095. [[CrossRef](#)]
22. Wang, Z.; Li, H. An Integrated Three-Port Bidirectional DC–DC Converter for PV Application on a DC Distribution System. *IEEE Trans. Power Electron.* **2012**, *28*, 4612–4624. [[CrossRef](#)]
23. Wu, H.; Xu, P.; Hu, H.; Zhou, Z.; Xing, Y. Multiport Converters Based on Integration of Full-Bridge and Bidirectional DC–DC Topologies for Renewable Generation Systems. *IEEE Trans. Ind. Electron.* **2013**, *61*, 856–869. [[CrossRef](#)]
24. Hintz, A.; Prasanna, U.R.; Rajashekar, K. Novel Modular Multiple-Input Bidirectional DC–DC Power Converter (MIPC) for HEV/FCV Application. *IEEE Trans. Ind. Electron.* **2014**, *62*, 3163–3172. [[CrossRef](#)]

